7-26-2022

Shear turbulence in the high-wind Southern Ocean using direct measurements

Laur Ferris
Virginia Institute of Marine Science

Carole Anne Clayson

Donglai Gong
Virginia Institute of Marine Science

et al

Recommended Citation

Ferris, Laur; Clayson, Carole Anne; Gong, Donglai; and et al, Shear turbulence in the high-wind Southern Ocean using direct measurements (2022). *Journal of Physcial Oceanography*.
doi: 10.1175/JPO-D-21-0015.1

Shear turbulence in the high-wind Southern Ocean using direct measurements

Laur Ferris,[a,c] Carole Anne Clayson,[b] Donglai Gong,[a] Sophia Merrifield,[c] Emily L. Shroyer,[d] Madison Smith,[e] Louis St. Laurent [e]

[a] *Virginia Institute of Marine Science - William & Mary, Gloucester Point, Virginia*

[b] *Woods Hole Oceanographic Institution, Woods Hole, Massachusetts*

[c] *Scripps Institution of Oceanography – University of California San Diego, La Jolla, California*

[d] *Office of Naval Research, Washington, D.C.*

[e] *Applied Physics Laboratory - University of Washington, Seattle, Washington*

Corresponding author: Laur Ferris, lferris@washington.apl.edu

File generated with AMS Word template 1.0

Early Online Release: This preliminary version has been accepted for publication in *Journal of Physical Oceanography*, may be fully cited, and has been assigned DOI 10.1175/JPO-D-21-0015.1. The final typeset copyedited article will replace the EOR at the above DOI when it is published.

ABSTRACT

The ocean surface boundary layer is a gateway of energy transfer into the ocean. Wind-driven shear and meteorologically forced convection inject turbulent kinetic energy into the surface boundary layer, mixing the upper ocean and transforming its density structure. In the absence of direct observations or the capability to resolve sub-grid scale 3D turbulence in operational ocean models, the oceanography community relies on surface boundary layer similarity scalings (BLS) of shear and convective turbulence to represent this mixing. Despite their importance, near-surface mixing processes (and ubiquitous BLS representations of these processes) have been under-sampled in high energy forcing regimes such as the Southern Ocean. With the maturing of autonomous sampling platforms, there is now an opportunity to collect high-resolution spatial and temporal measurements in the full range of forcing conditions. Here, we characterize near-surface turbulence under strong wind forcing using the first long-duration glider microstructure survey of the Southern Ocean. We leverage these data to show that the measured turbulence is significantly higher than standard shear-convective BLS in the shallower parts of the surface boundary layer and lower than standard shear-convective BLS in the deeper parts of the surface boundary layer; the latter of which is not easily explained by present wave-effect literature. Consistent with the CBLAST (Coupled Boundary Layers and Air Sea Transfer) low winds experiment, this bias has the largest magnitude and spread in shallowest 10% of the actively mixing layer under low-wind and breaking wave conditions, when relatively low levels of turbulent kinetic energy (TKE) in surface regime are easily biased by wave events.

SIGNIFICANCE STATEMENT

Wind blows across the ocean, turbulently mixing the water close to the surface and altering its properties. Without the ability to measure turbulence in remote locations,

Accepted for publication in *Journal of Physical Oceanography.* DOI 10.1175/JPO-D-21-0015.1.

oceanographers use approximations called "boundary layer scalings" (BLS) to estimate the amount of turbulence caused by the wind. We compared turbulence measured by an underwater robot to turbulence estimated from wind speed to determine how well BLS performs in stormy places. We found that in both calm and stormy conditions, estimates are 10 times too large closest to the surface and 10 times too small deeper within the turbulently mixed surface ocean.

1. Introduction

The surface boundary layer is the gateway for heat, momentum, and gas transfer between the atmosphere and interior ocean. Turbulent kinetic energy (TKE) injected into the upper ocean boundary layer, together with the surface buoyancy flux, directly affects the depth of mixing, controls water mass transformation, and mixes water to increase potential energy of the upper ocean structure (at the expense of TKE). As the only sector of the global ocean that connects all three major ocean basins through the meridional overturning circulation (MOC), the Southern Ocean is an especially important site of water mass transformation. Buoyancy forcing through air-sea exchange and interior mixing driven by internal waves transforms North Atlantic Deep Water (NADW) first into Subantarctic Mode Water (SAMW) and eventually into Antarctic Intermediate Water (AAIW) (Abernathey et al., 2016). The Scotia Sea east of the Drake Passage is believed to be a critical site of SAMW and AAIW modification and subduction (Talley, 1996; Sallée et al., 2010), but little is known about the formation of these water masses. Despite its importance, mixing processes in the Southern Ocean have been under-sampled, largely due to its remote location and severe conditions.

An autonomous profiling glider program called Autonomous Sampling of Southern Ocean Mixing (AUSSOM) was conducted in the Drake Passage region between the end of Austral Winter and the beginning of Austral Spring in 2017-2018. AUSSOM represents the

Accepted for publication in *Journal of Physical Oceanography.* DOI 10.1175/JPO-D-21-0015.1.

first extended glider deployment in the Drake Passage region of the ACC (Fig. 1) and is the longest continuous glider microstructure record ever collected. Unlike shipboard methods, gliders remain deployed for months at a time sampling though all sea states, thus it is a first opportunity to understand turbulent dissipation rate and mixing variations in the Polar Front (PF) of the Southern Ocean though a full range of atmospheric forcing conditions. The high spatial resolution and temporal extent of this dataset is also an opportunity to understand the performance of boundary layer similarity scaling (BLS) through the full range of meteorological forcing.

Much of the energy for turbulent mixing is injected into the surface mixed layer by a combination of buoyancy flux (convection), wind-driven shear flow, and wind-forced surface gravity waves (wave breaking and Langmuir circulation) (Mackinnon et al., 2013). Due to the inherent challenges of observation and representation of turbulence, the community relies on similarity scaling to estimate surface boundary layer turbulence in a variety of observational, analytical, and modeling pursuits; operational models such as HYCOM and ROMS utilize similarity scaling embedded in K-Profile Parameterization (KPP) mixing algorithms (Monin & Obukov, 1954; Large et al., 1994). Turbulence parameterizations based on law-of-the-wall BLS are common in models (Umlauf et al., 2005), as well as analytical and observational studies. BLS leverages fundamental results for fluid behavior at a boundary to estimate the turbulent dissipation caused by shear and convection, and is a simplification of the full TKE budget. The TKE budget, assuming the ocean is locally in steady state such that TKE per unit volume is constant, can be described in horizontally homogenous form $[m^2 s^{-3}]$ by

$$0 = -\frac{1}{\rho_o}\frac{\partial}{\partial z}\langle wp\rangle + \nu\frac{\partial^2}{\partial z^2}\mathrm{k} - \frac{\partial}{\partial z}\langle w\mathrm{k}\rangle - \langle uw\rangle\frac{dU}{dz} - \epsilon - \frac{g}{\rho_0}\langle \rho w\rangle \qquad \text{(Eq. 1)}$$

where (u, v, w) are turbulent velocity components, $\mathrm{k} = (\langle u^2\rangle + \langle v^2\rangle + \langle w^2\rangle)/2$ is the TKE, $\langle\_\rangle$ denotes an averages, p is the pressure fluctuation, ν is kinematic viscosity, dU/dz is

Accepted for publication in *Journal of Physical Oceanography.* DOI 10.1175/JPO-D-21-0015.1.

vertical shear of the mean flow velocity, g is gravity, and $\rho = -\rho_0 \alpha T' - \beta S'$ is the density fluctuation due to temperature and salinity fluctuations T' and S'. The terms on the right-hand side are (1) pressure-driven divergence of vertical kinetic energy flux, (2) viscous divergence of vertical kinetic energy flux, (3) vertical turbulent transport, (4) shear production, (5) dissipation rate, and (6) buoyancy production. Just outside the region closest to the boundary where viscous effects dominate (the viscous sublayer), there exists[1] a logarithmic layer (or inertial sublayer) in which the turbulence budget is typically approximated as a first-order balance between shear production, dissipation, and buoyancy (terms 4-6). However, there are several issues with this simplification, which neglects wave effects and boundary sources; in the real surface boundary layer, there is addition production due to Stokes shear, and neither variety of shear is necessarily aligned with the momentum flux $\langle uw \rangle$. Several past works have explored these additions (Agrawal et al., 1992; Sutherland et al., 2013; 2014; 2016; D'Asaro et al., 2014; Fox-Kemper et al., 2022).

To develop BLS, the transfer of horizontal momentum in the x direction by fluctuations in vertical velocity is assumed to be constant (Thorpe, 2005) and dominated by fluctuations in velocity rather than density such that Reynolds stress in the logarithmic layer is also assumed to be constant, $\tau/\rho_o = -\rho_o \langle uw \rangle$. This shear-dominated simplification of (Eq. 1) is:

$$\epsilon = (\tau/\rho_o) dU/dz \qquad \text{(Eq. 2)}$$

[1] In reality, this "logarithmic layer" is logarithmic only when shear production exactly balances dissipation.

Friction velocity (of the *water* at the boundary) is given by $u_* = \sqrt{(}\tau/\rho_o)$ where τ is wind stress and ρ_o is water density at the surface. When assuming that viscous effects are negligible in the logarithmic layer, dimensional grounds demand $dU/dz = \phi(z)u_*/kz$ where $k = 0.41$ is von Karman's constant (Thorpe, 2005). By assuming a perfect logarithmic layer and constant shear, the similarity structure function[2] is taken to be $\phi(z) \equiv 1$. Substituting into (Eq. 2) gives the principal equation for BLS of shear turbulence

$$\epsilon = -\frac{u_*^3}{kz} \qquad \text{(Eq. 3)}$$

In the presence of convection induced by buoyancy flux, (Eq. 3) is adapted to include the effects of buoyancy flux (J_b). One such adaptation (Lombardo & Gregg, 1989) based on similarity scaling of the atmospheric boundary layer is given in Table 1, where buoyancy production is represented as a contact function of surface flux $cJ_b = -g\langle\rho' w\rangle$, where c is a constant between 0 and 1. It is defined using the ratio of the Monin-Obukhov length scale $L_{MO} = -{u_*}^3/(kJ_b)$ (the depth at which the effects of wind-driven shear are equivalent to convection in turbulent flows) and the actively mixing layer (AML, the vertical extent of active turbulence, given in negative meters). L_{MO}, which is negative in destabilizing conditions, describes the scale inside of which turbulence generated by wind-driven shear dominates that generated by convection. If the AML is much less than L_{MO} or $L_{MO} > 0$, it is

[2] In the presence of penetrating radiation and Stokes shear production, similarity structure functions are no longer governed by the same systems of equations as in Monin-Obukhov theory. An excellent review of this topic is provided by Fox-Kemper et al. (2022).

Accepted for publication in *Journal of Physical Oceanography.* DOI 10.1175/JPO-D-21-0015.1.

a wind-dominated regime and convection is neglected. If the AML is significantly smaller than the L_{MO}, it is a convection-dominated regime and wind is neglected. Lombardo & Gregg (1989) tested BLS during mild-to-moderate winds, focusing on times with when the ocean steadily lost buoyancy to the atmosphere such that convection significantly contributed to dissipation.

Observations of turbulent dissipation are globally sparse (Waterhouse et al., 2014). The Southern Ocean has been noted as a location believed to exhibit large biases in mixed layer depth in climate models (e.g. CESM; CCSM, Danabasoglu et al., 2012). Here, we describe direct observation of boundary layer turbulence from AUSSOM using a framework of boundary layer scalings derived from wind and buoyancy forcing. This study focuses on the surface AML and its parameterization across the full range of wind forcing (up 20 m/s or ~40 knots), and it is the first step in a larger effort to combine BLS with satellite data products to provide a time-varying estimate of upper ocean mixing in the Southern Ocean. Understanding the physical processes and associated parameterizations for turbulent mixing in the surface mixed layer is critical for (1) understanding energy transfer into the mixed layer, (2) improving OSBL flux schemes embedded in circulation models, and (3) expanding turbulence estimations to satellite remote sensing platforms.

2. Methods

a. Glider observations

A Teledyne Webb Research Slocum glider equipped with a Rockland Scientific MicroRider was used to collect a 6-week record of upper-ocean turbulence spanning 800 km from the Shackleton Fracture Zone to the Falkland Plateau (Fig. 1). This glider-based methodology of measuring turbulence is well-documented in published literature (Fer et al.,

Accepted for publication in *Journal of Physical Oceanography.* DOI 10.1175/JPO-D-21-0015.1.

2014; St Laurent & Merrifield, 2017; Zippel et al., 2021). The glider was deployed at 58°S, 64°W at the southern edge of the Polar Front (PF) on 16 November 2017 from the R/V Laurence M. Gould, sampled for 60 days until 12 January 2018 when sensing disabled to preserve battery, and was recovered near Port Stanley, Falkland Islands on 5 February 2018. The dataset is one of the largest microstructure datasets ever collected, totaling over 3028 CTD profiles and 932 microstructure profiles from 0-350 meters (totaling approximately 300,000 meters of microstructure profiles in 60 days). For context, DIMES (Diapycnal and Isopycnal Mixing Experiment in the Southern Ocean) collected 800,000 meters of profiles over 5 years, 8 cruises, and 1 year of ship time. It is likely the most ever microstructure collected by a single instrument system.

The MicroRider, a glider-based sensor package for making direct turbulence measurements, was used for AUSSOM. In general, direct measurement of turbulence from a free fall platform assumes 3-D isotropy, which allows viscous dissipation (ϵ) of turbulent kinetic energy to be approximated by

$$\epsilon = \left(\frac{15}{2}\right) \nu \langle (du'/dz')^2 \rangle \qquad \text{(Eq. 4)}$$

where z' is the coordinate aligned with the shear probes, u' is the water velocity component normal to z', and $du'/dz' = (\partial u'/\partial t)(\partial t/\partial z') = (\partial u'/\partial t)/V$. Here ν is the molecular kinematic viscosity of water [~1×10^{-6}m^{2}s^{-1}] and $\partial u'/\partial t$ are velocity fluctuations measured by the shear probes. When using any package, velocity of the instrument through the water (V) is required to calculate turbulent dissipation. Glider microstructure differs from free-fall microstructure in that the velocity of shear probes through the water is not the same as its fall rate. It is possible to calculate vertical glider speed using a flight model (Merckelbach et al., 2019), but the pressure-derived vertical velocity W is sufficiently accurate for this application (Fer et al., 2014). The velocity [m/s] of

the glider through the water $V = W/sin(\phi + \alpha)$ is calculated using the vertical component of that velocity W and glide angle, where glide angle is the sum of pitch angle (ϕ) and the angle of attack (α) (St. Laurent & Merrifield, 2017). Vertical eddy diffusivity of density $K_\rho = \Gamma\langle\epsilon\rangle/\overline{N^2}$ is estimated using measured turbulent dissipation rate (ϵ), buoyancy frequency (N^2) calculated from CTD using adiabatic leveling, and an assumed efficiency factor of $\Gamma = 0.2$. We explore the collected dataset using the framework of convection-shear BLS: we implement BLS, compare to glider microstructure, and explore the differences between observed turbulence and BLS estimates of turbulence in the high-wind Southern Ocean.

b. Boundary layer similarity scaling

In the absence of direct meteorological measurements, we harness satellite data for records of meteorological forcing, which are required for buoyancy flux calculations. The buoyancy flux is calculated using

$$J_b = g[\frac{\alpha}{\rho c_p} Q_{tot} + \beta S_o (E - P)] \quad \text{(Eq. 5)}$$

where α and β are the expansion coefficients for heat and salinity, c_p is the specific heat of seawater, Q_{tot} is the total heat flux (SeaFlux CDR dataset [Clayson & Brown, 2016]), S_o is sea surface salinity (Copernicus product Global SSS/SSD L4 Processor V1.1), E is the evaporation rate (SeaFlux CDR), and P is precipitation (GPCP V1.3 Daily Rainfall). Friction velocity (u_*) is computed from surface radiation flux (CERES_SYN1deg_Ed4A), winds (CCMPv2), near-surface specific humidity (SeaFlux CDR), near-surface temperature (SeaFlux CDR), and SST (SeaFLUX Ocean CDR) using the COARE Met Flux Algorithm v3.5 (Edson et al., 2013). Windsea significant wave height (H_s) is obtained from the Copernicus Global Ocean Waves Multi Year product, which is a global wave reanalysis on a 1/5° grid, at a 3-hourly temporal resolution. Wave steepness (H/L) is calculated from

Copernicus Global Ocean Waves Multi Year product (1/5° grid, at a 3-hourly temporal resolution) using wind wave mean period (T) and significant wave height from wind and swells (H) using $L = 2\pi H/gT^2$, and turbulent Langmuir number is calculated $La_t = (u_*/u_{s0})^{1/2}$ where u_{s0} is surface velocity of Stokes drift. Direct wave observations are not available.

The determination of AML depth and MLD are demonstrated by Figure 2. Whereas the AML is defined by elevated turbulent dissipation, the MLD is defined by homogenous density. AML identification is completed for 932 microstructure profiles using a simple algorithm. The steps for each microstructure profile are to: (a) Find the depth at which a log-linear fit of surface (upper 100 meters) ϵ falls to an empirically determined background $\epsilon = 10^{-8}$ W/kg (Fig. 2d). (b) Discard obviously wrong fits (~0.75% of profiles) using automatic checks. (c) Interpolate good AML depths. A critical step in the process is excluding enhanced turbulence at depth that is unrelated to direct surface (wind or buoyancy) forcing; restricting polynomial fitting to the upper 100m—empirically selected to focus on surface-forced turbulence—avoids mixing events that are unrelated to surface boundary layer physics (e.g. internal wave and forward cascade). While the polynomial coefficients are determined from ϵ data in the the upper 100m the resulting fit is allowed to extend below this depth. The result is a working AML depth dataset that avoids deep (e.g. internal wave-related) mixing (Fig 2a). MLD is from glider CTD using a surface-density difference criterion of $\Delta\rho = 0.03$ kg/m^3 and $\Delta T = 0.2$°C, where the two estimates of MLD are compared for sensitivity and shallower estimate is generally used (Dong et al., 2008). AML depth can change on a faster (~20m/hr) timescale than the mixed layer depth (MLD); turbulence of the AML works to homogenize the water column, producing a mixed layer.

Upon inspection (Fig. 3) it is clear that our study is wind dominated (with less than 1% of cases invoking buoyancy flux into BLS) such that we can neglect convection. Two versions of boundary layer similarity scaling (BLS) are implemented (Fig. 4). The standard version (using COARE variables) applies the full wind and buoyancy flux scaling (Table 1) using u_* and J_b. We also implemented a simplified version of BLS using solely u_* interpolated from CCMPv2, the easily-accessible wind product available from Remote Sensing Systems (http://www.remss.com/). With close agreement relative to the biases, the reader may consider for themself (Fig. 4b, 4d) when it might be appropriate to just use the simplified version of BLS in wind-dominated situations. However, the rest of our paper uses the standard version of BLS.

Individual microstructure and synchronous BLS profiles were also integrated (Eq. 6) to obtain the dissipated power associated with the observations and scaled estimates (Fig. 4d).

$$\Phi = \int_{z_{AML}}^{z_{min}} \rho \epsilon dz \qquad \text{(Eq. 6)}$$

Turbulence observations and estimates were temporally averaged prior to calculating the observed bias in BLS, $log_{10}(\epsilon_{BLS}/\epsilon)$. Because the timescale of mixing events is shorter than the temporal resolution (6 hours) of the CCMPv2 wind data, individual microstructure profiles must be averaged over some timescale (long enough that the wind product adequately represents mean turbulent dissipation but short enough to capture changing conditions) to produce useful comparison to wind-based BLS profiles. A 14.5-hour (inertial period) averaging interval is used. Surface boundary layer turbulence is normalized by the AML depth and temporally averaged with adjacent profiles using 30 vertical bins. Finally, polynomial fits are used to document the structure of the observed bias.

3. Results

Accepted for publication in *Journal of Physical Oceanography.* DOI 10.1175/JPO-D-21-0015.1.

a. Comparison to turbulence estimates of standard shear-convective BLS

Overall, glider survey revealed interesting subsurface physics, observing elevated turbulent dissipation rates ($\epsilon = 10^{-7}$ W/kg) for the entire duration for which the glider sampled the core of the Polar Front (Fig. 1b). Glider CTD observed some salt fingering and double diffusive staircases north of the PF (consistent with Merrifield et al., 2016) and sporadic diffusive/oscillatory convection (Ferris et al., 2020). Subsurface phenomena are examined in Ferris (2021). Convection forced by buoyancy flux played a minimal role in forcing the AML during the study (Fig. 3), with buoyancy rarely removed from the upper ocean and energy for near-surface mixing predominately supplied by wind stress. An analysis of time-averaged microstructure and turbulence profiles estimated using boundary layer scaling (Lombardo & Gregg, 1989) demonstrates that the BLS turbulent dissipation in the shallowest depths is higher than predicted by the BLS paradigm and turbulent dissipation deeper within the AML is lower than predicted by BLS (see Fig. 5 for an example profile), consistent with Merrifield's (2016) bulk analysis of tow-yo VMP transects from DIMES US5.

A section of this bias is shown in Fig. 6c, with blue hues (red hues) indicating underprediction (overprediction) of turbulence in the surface boundary layer, with underprediction of near-surface TKE dissipation rates by up to 4 orders of magnitude. The vertical extent of this underprediction varies in depth, with three strong events lagging 2-3 days after intense storms; these will be revisited in the Discussion. Several cases do not have the characteristic bias profile (Fig. 6b, bright red hues at the surface), which are associated with either instances in which there are fewer than 5 microstructure profiles available within the 14.5-hour interval for averaging (21 November and 30 November), or profiles overlying the continental rise or shelf (after 22 December). Few profiles available for averaging is an

obvious factor in inconsistent BLS bias due to higher statistical uncertainty (see Moum [2021] for a recent review). The similarity of observed turbulence to BLS does not depend on whether wind inflection (wind speed increasing or decreasing), nor proximity to Polar Front.

Before documenting the character and magnitude of the bias (Fig. 6c), we place several restrictions on the data. Profiles are excluded (181 profiles or ~19.4%) because (a) the profile does not have a recognizable AML, (b) the profile is over the continental rise or shelf and thus likely contaminated by elevated bottom boundary layer mixing, or (c) there are no measurements in an entire vertical bin of a temporal average. Profiles are normalized by AML depth and measurements beyond the AML are omitted from analysis. After quality control, bias is quantified in two ways (Fig. 7b): a full dataset polynomial fit, and polynomial fit for the mean $\mu(z) = ln(\epsilon_{BLS}/\epsilon)$and the standard deviation $\sigma(z)$ of the depth-dependent probability distribution function (PDF) fit to individual PDF computed from a moving vertical window. Polynomial fits $\hat{\xi}(z)$ of $ln(\epsilon_{BLS}/\epsilon)$ and its standard deviation are given by (Eq. 7):

$$\hat{\xi}(z) = \xi_5\hat{z}^5 + \xi_4\hat{z}^4 + \xi_3\hat{z}^3 + \xi_2\hat{z}^2 + \xi_1\hat{z} + \xi_0 \quad \text{(Eq. 7)}$$

where $\hat{z} = z/AML$ is the magnitude of the distance from the surface and coefficients are provided in Table 2. We used a 5th-degree polynomial because it best described this particular dataset; but do not suggest there is a physical reason that future adaptations to BLS should take this form. Depth regimes for Fig. 7a are partitioned by the zero crossing of bias polynomials (Fig. 7b), $\hat{z} = 0.1$, which is the same regardless of whether bias is defined $log_{10}(\epsilon_{BLS}/\epsilon)$ or $ln(\epsilon_{BLS}/\epsilon)$. The near-surface AML exhibits a larger standard deviation in bias (Fig. 7a) than the deeper AML, suggesting wave dynamics at the air-sea interface are a significant factor.

Accepted for publication in *Journal of Physical Oceanography.* DOI 10.1175/JPO-D-21-0015.1.

b. Controls on bias in two depth regimes

Next, we examine controls on the normalized bias (Fig. 8-10) including friction velocity (u_*), windsea significant wave height (H_s), and turbulent Langmuir number (La_t). u_* and H_s mirror each other such that they are a reasonable proxy for one another. We separate turbulence estimates into a near-surface regime and a deeper regime as in Fig. 7a. We observe that wind speed (Fig. 8) has an inverse effect on the magnitude of near-surface underestimation (μ = -0.574 low wind vs. μ = 0.099 high wind), with *larger biases in low wind conditions*; but direct effect on the magnitude of deep overestimation (μ = 0.345 low wind vs. μ = 0.491 high wind). Wave breaking (Fig. 9) has a direct effect on the magnitude of near-surface underestimation (μ = -0.091 non-breaking vs. μ = -0.563 breaking waves), with *larger biases in breaking wave conditions*; but inverse effect on the magnitude of deep overestimation (μ = 0.451 non-breaking vs. μ = 0.354 breaking waves). Conditions conducive to Langmuir circulation (Fig. 10) have a direct effect on the magnitude and sign of near-surface underestimation (μ = 0.146 Langmuir inactive vs. μ = -0.396 Langmuir active) and an inverse effect on the deep overestimation (μ = 0.517 Langmuir inactive vs. μ = 0.377 Langmuir active). Langmuir circulation is unlikely the principle physical process at work (out of those unrepresented by BLS) because Langmuir circulation would be expected redistribute turbulence from the near-surface to the deeper AML, causing a tendency towards overestimation in the near-surface and underestimation at depth (the opposite of what we observed).

c. Relationship of mixed layer development and the Polar Front

We observe an interesting relationship between frontal hydrography and shallow mixing (Fig. 11). The glider crossed south into the PF on 11/28, marking a sharp reduction in salinity

Accepted for publication in *Journal of Physical Oceanography.* DOI 10.1175/JPO-D-21-0015.1.

(Fig. 1b) and mixed layer depth (Fig. 2b). This is associate with a transition in the relationship between MLD and AML (Fig 11d). North of the PF the AML rarely develops beyond the mixed layer; TKE erodes the base of MLD, mixing away this interface. But beyond the PF in the cold/fresh/dense Southern Ocean waters the AML routinely develops beyond the MLD; there is with little compliance from the mixed layer itself (Fig. 2). This could be due to greater stratification resisting mixed layer deepening (despite churning by TKE), or intense lateral density gradients within the PF core creating stability and preventing convection. The relationship between water masses and the AML: MLD ratio is complicated by seasonal transition from winter to summer, increasing stratification of the upper Southern Ocean, similar to that observed by du Plessis et al., (2019). A deepening of isopycnals occurs during the 6 December and 12 December storm events (Fig. 11), as well as following Langmuir-circulation-favorable conditions on 17 December. The influence of both the Polar Front and seasonal transition on mixing dynamics are worthy of future investigation.

4. Discussion

a. Influence of waves

Throughout AUSSOM buoyancy flux played a minimal role in deepening the AML in the Drake Passage and Scotia Sea region (usually extracting energy and reducing its development), with energy for near-surface mixing supplied almost solely by wind stress. Focusing our discussion on shear production, BLS likely underpredicts energy input into the near-surface ocean because it does include surface gravity wave breaking and/or TKE from alternative sources in the observed Southern Ocean environment. Our observations suggest BLS (Lombardo & Gregg, 1989) of shear turbulence in the Southern Ocean exhibit a systematic bias, underestimating (overestimating) turbulent dissipation rates in the shallower

Accepted for publication in *Journal of Physical Oceanography.* DOI 10.1175/JPO-D-21-0015.1.

(deeper) parts of the surface boundary layer. The magnitude of the near-surface underestimate is greatest when wind is mild (Fig. 8) and waves are breaking (Fig. 9). This is not surprising; the Lombardo & Gregg (1989) form of BLS is a rigid-boundary theory and assumes a TKE budget dominated by shear production, buoyancy production, and dissipation (Eq. 1). Contrary to the rigid-boundary paradigm, surface gravity waves are known to alter boundary layer structure within several significant wave heights of the surface (Agrawal et al., 1992); and our observations are not the first for which waves cause a departure from BLS theory. Gerbi et al. (2009) used a model and observations from the Coupled Boundary Layers and Air Sea Transfer (CBLAST) low winds experiment to find production alone was unable to balance dissipation (as in Eq.1) in the wave affected-surface layer, which lies above the logarithmic layer (Terray et al., 1996).

We have reproduced the Gerbi et al. (2009) finding in Fig. 12 using our measurements, which should produce identical statistics to those computed using an Eulerian platform (Derakhti et al., 2020). The inclusion of a transport term (representing wave breaking, nonlinear wave-turbulence interactions, and Langmuir turbulence) improved the model, though contributions of Langmuir turbulence were found unimportant relative to wave breaking (like our results, Fig. 9-10). Fox-Kemper et al. (2022) note that systematic inconsistencies arise when wind waves deviate in direction from the wind stress itself or propagate from a nonlocal generation site, which is worth mentioning given that our dataset contains a prominent wave presence. In the real ocean surface boundary layer, there is addition production due to Stokes drift (U_S) (McWilliams et al., 1997; Belcher et al. 2012) and shear is not necessarily aligned with the momentum flux $\langle uw \rangle$ (McWilliams et al., 2014) such that more updated representation of Eq. 1 with terms 1-3 neglected is:

$$0 = -\langle uw \rangle \frac{dU}{dz} F(U_S) F(z/L_{MO}) \cos A - \langle uw \rangle \frac{dU_S}{dz} \cos B - \epsilon - \frac{g}{\rho_0} \langle \rho' w \rangle + WBP \qquad \text{(Eq. 8)}$$

where angles A and B are the wind direction relative to the shear terms. In conditions where ϵ is strongly driven by the wave field and Stokes drift, surface gravity waves reduce the shear by a function of the Stokes drift $F(U_S)$ (Large, et al. 2019) and there is wave breaking production (WBP) such that Reynolds stress is realistically a decaying function of depth $F(z)$. A and B are rarely both near-zero, and A can exceed 90 degrees in some real ocean conditions due to varying wind direction, such that energy is extracted. In the absence of background velocity shear, we cannot evaluate the leftmost term of (Eq. 8) but evaluate $-\langle uw \rangle \frac{dU_s}{dz} \cos B$ to demonstrate the importance of Stokes shear production, with $\frac{dU_s}{dz}$ estimated from Craik (1985) using

$$U_s(z) \approx \frac{4\pi^2 a^2}{\lambda T} e^{4\pi z/\lambda} \quad \text{(Eq. 9)}$$

where $c = gT/(2\pi)$, and T is the wave period of the spectral peak and a is the amplitude of the primary swell. Near-surface underestimation (bias in the shallowest 10% of the AML) reduces from $\mu = -0.554$ to $\mu = -0.450$ overall (as in Fig. 7a), $\mu = -0.574$ to $\mu = -0.517$ in low-wind conditions and $\mu = 0.099$ to $\mu = 0.133$ in high wind conditions (as in Fig. 8), $\mu = -0.091$ to $\mu = -0.048$ in nonbreaking and $\mu = -0.563$ and $\mu = -0.510$ in breaking wave conditions (as in Fig. 9), and $\mu = -0.396$ to $\mu = -0.344$ in Langmuir active and $\mu = 0.146$ to $\mu = 0.177$ in Langmuir active conditions (as in Fig. 10); representing an improvement in all cases except high wind and Langmuir inactive conditions, when bias is positive to begin with. The deep overestimation worsens from $\mu = 0.960$ to $\mu = 1.111$ overall and in all cases, but this is unsurprising because we did not account for vertical decay due to $F(U_S)$. Notably, however, this representation does not explain the bias in our dataset. Deep overestimation events (Fig. 6c) would worsen if overall positive bias were made to accommodate $\langle uw \rangle$ decreasing from the surface) as in (Eq. 8).

Accepted for publication in *Journal of Physical Oceanography.* DOI 10.1175/JPO-D-21-0015.1.

Numerical modeling literature has aimed to understand the implications of breaking surface waves and Langmuir turbulence, which are not included in wall-bounded (standard shear-convective BLS) turbulence parameterizations and subgrid mixing schemes unless explicitly added (e.g. Kantha & Clayson, 2004). Belcher et al. (2012) concluded surface wave-forced Langmuir turbulence should be a dominant TKE source in the Southern Ocean, and several observational studies (D'Asaro et al., 2014; Sutherland et al., 2014) corroborate the importance of Langmuir circulation in turbulence generation. While the inclusion of Langmuir turbulence parameterization schemes in ocean general circulation models (OGCMs) produces mixed layers of 2-25% deeper in extratropical, weak-convection regions such as the austral summer Southern Ocean (Li et al., 2019), it is unclear to what extent Langmuir turbulence is mechanistically responsible for deeper mixed layers in the real ocean (D'Asaro, 2014). Sullivan et al. (2007) used large eddy simulation to find that the wave age c_p/u_{*a} (where c_p is phase speed of the spectral peak and u_{*a} is air friction velocity) impacted the near-surface mixing, with younger wave groups and higher wind speeds exhibiting a larger positive feedback with Langmuir turbulence and increases near-surface dissipation. To explore scalings leveraging these wave characteristics, we tested two alternative scalings in comparison to depth-integrated TKE (Fig. 13) including ones based on wave age ($F_1 = G_t u_*^3$, Craig & Banner, 1994) and wave-range effective speed ($F_2 = c_e u_*^2$, Gemmrich et al., 1994). Thomson et al., (2016) tested these scalings (albeit without consideration of buoyancy flux) and found that F_2 marginally had the best agreement with observations. Our data (Fig. 13) is inconsistent with their result; we find both scalings produce inflated energy levels relative to (Eq. 3). Even with bias, BLS performs 1-2 orders of magnitude better than alternative scalings based on wave age or wave-range effective speed.

Accepted for publication in *Journal of Physical Oceanography.* DOI 10.1175/JPO-D-21-0015.1.

Surface gravity wave breaking in the high-wind Southern Ocean environment violates a key assumption of BLS (that shear stress in the logarithmic layer is constant function of wind-imparted stress). However, this physical explanation alone is insufficient because near-surface bias is more severe during the mildest winds. While presence of nonlocally generated swell could be a factor, it is also possible that contributions from surface gravity waves are persistent but only noticeable in low-wind cases due to lower levels of TKE dissipation. The near-surface underestimation and deeper-AML overestimation is inherently coupled; energy lost in the near-surface will not reach the deeper AML, resulting in lower levels of turbulent dissipation than predicted. Near-surface underestimation by BLS is worse when there are breaking wave conditions and low wind-driven shear (Fig. 8-9), but the opposite effect is not seen in the deeper histograms suggesting there must be other physical processes at work.

b. Influence of sources other than breaking waves

A second physical explanation is that sources of turbulent kinetic energy (TKE) other than wind-driven shear significantly contribute to observed turbulent dissipation. Lombardo & Gregg (1989) assumes energy injection into the dissipative scale is accomplished by direct meteorological forcing (wind-driven shear and convection) in the surface boundary layer, but other processes such as Langmuir driven turbulence (discussed in Section 4a), shear instabilities, and submesoscale instabilities could be active in an intense wind-sheared frontal zone. As stated in Section 4a, our dataset does not support a dominant role of Langmuir-driven turbulence; generation and redistribution of TKE by Langmuir circulation cannot be the only additional source of TKE because the presence or absence of this mechanism does not explain deep underestimation events. Rather, it favors alternative (other than wind-driven) mechanisms such in Sutherland et al. (2016), who observed a wind-driven jet in the subtropical Atlantic during the SPURS (Salinity Processes in the Upper Ocean Regional

Accepted for publication in *Journal of Physical Oceanography.* DOI 10.1175/JPO-D-21-0015.1.

Study) to find that diurnal increase in stratification restricts vertical diffusion of wind stress and depth of momentum flux, increasing near-surface shear instability (an additional source of near-surface TKE). Mixing in the Antarctic Circumpolar Current (ACC) might be further complicated by the numerous other processes turbulently transforming the upper ocean, such as internal wave driven mixing (St. Laurent et al., 2012) and double diffusion (Merrifield et al., 2016). It should be emphasized that this second explanation is not a complete explanation by itself because it does not account for the lack of observed turbulence at depth in Fig. 7-10.

c. Impact of storms

We revisit the cause of the deeper underestimation events (Fig. 6c); restated, patches of elevated observed turbulence (blue hues) extending deeper into the AML which were not captured by BLS. There is some second-order dynamical effect; the timescale of this effect is much longer than the inertial period (~14.5 hours), and timescale for a storm system to pass the glider is less than one day. Glider depth-averaged current is comparable to ACC velocity (from Operational Mercator, Fig. 1) extracted along the track of the glider such that the platform is effectively Lagrangian; it is not the case that ACC velocity is advecting/distorting patches of turbulence (associated with wave breaking) faster than the glider such that they appear lagged in the turbulence record. A plausible physical mechanism explaining these deeper underestimation events is described in Dohan & Davis (2011); who observed a storm to excite near-inertial oscillations & currents (with their own additional shear), causing elevated mixing for 3 days after the storm itself. Wind direction turned with the direction of inertial rotation such that it resonantly excited the oscillations, and we similarly see a wind direction turn in the direction of inertial rotation (Fig. 6e) during storm events. An important question is why the TKE contribution shear instability in inertial currents would appear in BLS bias $log_{10}(\epsilon_{BLS}/\epsilon)$ as a *delayed* underestimation event and not immediately. During the

Accepted for publication in *Journal of Physical Oceanography.* DOI 10.1175/JPO-D-21-0015.1.

storm itself, the calculation of bias would be heavily buffered by the wind-forced shear turbulence, such that the secondary component would perhaps not become noticeable until the wind relented and only the current shear remained. As wind subsides, the contribution of mixing due to current shear would subside, both ϵ and ϵ_{BLS} become smaller and this additional contribution becomes more noticeable. We speculate that this mechanism could similarly create a delayed TKE contribution from the storms, though this cannot be confirmed with the available data.

5. Conclusion

We tested boundary layer scalings (BLS) from satellite data against direct measurements of TKE dissipation rate from a glider. We found that BLS underestimates turbulent dissipation in the near-surface and overestimates turbulent dissipation below the near-surface, consistent with Merrifield (2016). The structure of this bias is consistent across wind speeds in the lower 90% of the AML, but strongly contingent on wind speed in the upper 10% of the AML. In the near-surface AML, underestimation by BLS is larger in low wind conditions, breaking wave conditions, or when Langmuir circulation is active; however, in the deep AML, differences across wind and wave conditions are much less statistically significant. Explanations for this systematic bias are that: (1) The rigid-boundary paradigm does not account for surface gravity wave breaking and momentum loss in the high-wind Southern Ocean environment. (2) Sources of TKE other than wind-driven shear and buoyancy flux are contributing to dissipation; furthermore, Langmuir circulation alone cannot explain deep underestimation events. (3) Deep underestimation events are due to additional shear caused by storm-forced inertial currents (see Dohan & Davis, 2011). Despite these shortcomings, we found that BLS still outperforms alternative scalings (Craig & Banner, 1994; Gemmrich et al., 1994) based on wave age or wave-range effective speed, motivating its further

Accepted for publication in *Journal of Physical Oceanography.* DOI 10.1175/JPO-D-21-0015.1.

development. We built on the observational work of Lombardo & Gregg (1989) by showing a wind-dominated regime is characterized by significant momentum loss, alternative TKE sources, and significantly greater turbulent dissipation in the near-surface than predicted by BLS. Representing the physical processes responsible for this near-surface TKE dissipation is critical for understanding mixed layer dynamics and water mass transformation when wind-driven shear dominates convection in the global ocean. AUSSOM tested boundary layer scaling in high-wind, non-convective conditions, but future investigations covering the full wind and buoyancy forcing parameter space are needed; especially involving cases where both wind-driven shear and buoyancy loss are significant.

Acknowledgments.

This paper is VIMS Contribution No.xxxx. Computational resources were provided by the VIMS Ocean-Atmosphere & Climate Change Research Fund. AUSSOM was supported by the OCE Division of the National Science Foundation. We thank the Captain and crew of the R/V Gould for their excellent support during the field program, and Justin Shapiro for the recovery mission. We also thank the editor and two anonymous reviewers whose invaluable feedback greatly improved the paper. This study has been conducted using E.U. Copernicus Marine Service Information. CCMP Version-2.0 vector wind analyses are produced by Remote Sensing Systems.

Data Availability Statement.

All glider data used in the paper will be shared at microstructure.ucsd.edu, the NSF-funded Microstructure Database. The COARE 3.5 algorithm and its associated data products are publicly available. This includes surface radiation data from the CERES project (https://ceres.larc.nasa.gov/products-info.php?product=SYN1deg), CCMPv2 winds (www.remss.com; Wentz et al., 2015), near-surface temperature and humidity from SeaFlux

CDR (https://www.ncdc.noaa.gov/cdr/atmospheric/ocean-near-surface-atmospheric-properties; Clayson et al., 2016b), sea surface temperature from SeaFlux Ocean CDR (https://www.ncdc.noaa.gov/cdr/oceanic/sea-surface-temperature-whoi; Clayson et al., 2016a), GPCP V1.3 daily rainfall product (https://www.ncdc.noaa.gov/cdr/atmospheric/precipitation-gpcp-daily; Adler et al., 2017), and aforementioned CMEMS products.

REFERENCES

Abernathey, R. P., I. Cerovecki, P. R. Holland, E. Newsom, M. Mazloff, and L. D. Talley, 2016: Water-mass transformation by sea ice in the upper branch of the Southern Ocean overturning. *Nat. Geosci.* **9,** 596-601.

Adler, R., J.-J. Wang, M. Sapiano, G. Huffman, D. Bolvin, E. Nelkin, and NOAA CDR Program, 2017: Global Precipitation Climatology Project (GPCP) Climate Data Record (CDR), Version 1.3 (Daily). NOAA National Centers for Environmental Information, doi:10.7289/V5RX998Z.

Agrawal, Y. C., E. A. Terray, M. A. Donelan, P. A. Hwang, A.J. Williams, W. M. Drennan, K. K. Kahma, and S. A. Krtaigorodskii,1992: Enhanced dissipation of kinetic energy beneath surface waves. *Nature*, **359**, 219-220.

Belcher, S. E., Grant, A.L., Hanley, K. E., Fox- Kemper, B., Van Roekel, L., Sullivan, P.P., Large, W. G., Brown, A., Hines, A., Calvert, D., Rutgersson, A., 2012: A global perspective on Langmuir turbulence in the ocean surface boundary layer. *Geophys. Res. Lett.*, **39**.

Clayson, C. A., and J. Brown, 2016: NOAA Climate Data Record Ocean Surface Bundle (OSB) Climate Data Record (CDR) of Ocean Heat Fluxes, Version 2. Climate Algorithm

Theoretical Basis Document (C-ATBD). NOAA National Center for Environmental Information, doi:10.7289/V59K4885.

Clayson, C. A., J. Brown, and NOAA CDR Program, 2016a: NOAA Climate Data Record (CDR) of Sea Surface Temperature - WHOI, Version 2. NOAA National Climatic Data Center. doi:10.7289/V5FB510W.

Clayson, C. A., J., Brown, and NOAA CDR Program 2016b: NOAA Climate Data Record Ocean Surface Bundle (OSB) Climate Data Record (CDR) of Ocean Near Surface Atmospheric Properties, Version 2. NOAA National Center for Environmental Information, doi:doi:10.7289/V55T3HH0.

Craig, P. D. and M. L. Banner, 1994: Modeling wave-enhanced turbulence in the ocean surface layer. *J. Phys. Oceanogr.*, **24**, 2546-2559.

Craik, A. D., 1988: *Wave interactions and fluid flows*. Cambridge University Press.

D'Asaro, E. A., 2014: Turbulence in the upper-ocean mixed layer. *Annu. Rev. Mar. Sci.*, **6,** 101-115.

D'Asaro, E. A., J. Thomson, A. Y. Shcherbina, R. R. Harcourt, M. F. Cronin, M. A. Hemer, and B. Fox-Kemper, 2014: Quantifying upper ocean turbulence driven by surface waves. *Geophys. Res. Lett.*, **41,** 102-107.

Danabasoglu, G., and Coauthors, 2012: The CCSM4 Ocean Component. *J. Climate*, **25,** 1361-1389.

Derakhti, M., J. Thomson, and J. T. Kirby, 2020: Sparse Sampling of Intermittent Turbulence Generated by Breaking Surface Waves. *J. Phys. Oceanogr.*, **50,** 867-885.

Dohan, K., and R. E. Davis, 2011: Mixing in the Transition Layer during Two Storm Events. *J. Phys. Oceanogr.*, **41,** 42-66.

Dong, S., J. Sprintall, S. T. Gille, and L. Talley, 2008: Southern Ocean mixed-layer depth from Argo float profiles. *J. Geophys. Res.*, **113**.

du Plessis, M., S. Swart, I. J. Ansorge, A. Mahadevan, and A. F. Thompson, 2019: Southern Ocean Seasonal Restratification Delayed by Submesoscale Wind–Front Interactions. *J. Phys. Oceanogr.*, **49,** 1035-1053.

Edson, J. B., and Coauthors, 2013: On the exchange of momentum over the open ocean. *J. Phys. Oceanogr.*, **43**, 1589-1610.

Fer, I., A. K. Peterson, and J. E. Ullgren, 2014: Microstructure Measurements from an Underwater Glider in the Turbulent Faroe Bank Channel Overflow. *J. Atmos. Ocean. Technol.*, **31,** 1128-1150.

Ferris, L., 2021: Across-scale energy transfer in the Southern Ocean. Doctoral dissertation, Dept. of Physical Sciences, Virginia Institute of Marine Science – William & Mary, 190 pp.

Ferris, L. N., D. Gong, T. Ijichi, S. T. Merrifield, J. Shapiro, L. St. Laurent, 2020: Turbulent Dissipation Rate and Mixing Variations in the Polar Front of the Southern Ocean. *Ocean Sciences Meeting 2020*, San Diego, CA, American Geophysical Union, PS51A-04, https://agu.confex.com/agu/osm20/meetingapp.cgi/Paper/648069.

Fox-Kemper, B., Johnson, L., Qiao, F (2022): Ocean Near-Surface Layers, *Ocean Mixing*, Elsevier.

Gemmrich, J. R., T. D. Mudge, and V. D. Polonichko, 1994: On the energy input from wind to surface waves. *J. Phys. Oceanogr.*, **24**, 2413-2417.

Gerbi, G. P., J. H. Trowbridge, E. A. Terray, A. J. Plueddemann, and T. Kukulka, 2009: Observations of Turbulence in the Ocean Surface Boundary Layer: Energetics and Transport. *J. Phys. Oceanogr.*, **39,** 1077-1096.

Hwang, P. A., 2009: Estimating the effective energy transfer velocity at air-sea interface. *J. Geophys. Res.*, **114**.

Kantha, L. H., and C. Anne Clayson, 2004: On the effect of surface gravity waves on mixing in the oceanic mixed layer. *Ocean Modelling*, **6,** 101-124.

Large, W. G., J. C. McWilliams, and S. C. Doney, 1994: Oceanic vertical mixing: A review and a model with a nonlocal boundary layer parameterization. *Rev. Geophys.*, **32**, 363-403.

Large, W. G., Patton, E. G., DuVivier, A. K., Sullivan, P. P., Romero, L., 2019: Similarity theory in the surface layer of large-eddy simulations of the wind-, wave-, and buoyancy-forced southern ocean. Journal of Physical Oceanography, **49,** 2165-2187.

Li, Q., and Coauthors, 2019: Comparing Ocean Surface Boundary Vertical Mixing Schemes Including Langmuir Turbulence. *J. Adv. Model.*, **11,** 3545-3592.

Lombardo, C. P. and M. C. Gregg, 1989: Similarity scaling of viscous and thermal dissipation in a convecting surface boundary layer. *J. Geophys. Res. Oceans*, **94**, 6273-6284.

McWilliams, J. C., Huckle, E., Liang, J., Sullivan, P. P., 2014: Langmuir turbulence in swell. *J. Phys. Oceanogr*, **44**, 870-890.

McWilliams, J. C., Sullivan, P. P., & Moeng, C. H., 1997: Langmuir turbulence in the ocean. *J. Fluid Mech.*, **334**, 1-30.

Accepted for publication in *Journal of Physical Oceanography.* DOI 10.1175/JPO-D-21-0015.1.

MacKinnon, J., L. St. Laurent, and A. C. Naveira Garabato, 2013: Diapycnal Mixing Processes in the Ocean Interior. *Ocean Circulation and Climate - A 21st Century Perspective*, Academic Press, 159-183.

Merckelbach, L., A. Berger, G. Krahmann, M. Dengler, and J. R. Carpenter, 2019: A dynamic flight model for Slocum gliders and implications for turbulence microstructure measurements. *J. Atmos. Ocean. Technol.*, **36**, 281-296.

Merrifield, S. T., 2016: Mechanisms for enhanced turbulence in the Drake Passage Region of the Southern Ocean. Doctoral dissertation, Massachusetts Institute of Technology, 134 pp.

Merrifield, S. T., L. S. Laurent, B. Owens, A. M. Thurnherr, and J. M. Toole, 2016: Enhanced Diapycnal Diffusivity in Intrusive Regions of the Drake Passage. *J. Phys. Oceanogr.*, **46,** 1309-1321.

Monin, A. S. and A. M. Obukhov, 1954: Basic laws of turbulent mixing in the surface layer of the atmosphere. *Contrib. Geophys. Inst. Acad. Sci. USSR*, **151**, 163-187.

Moum, J. N., 2021. Variations in Ocean Mixing from Seconds to Years. *Annu. Rev. Mar. Sci.*, **13**, 201-226.

Sallée, J.-B., K. Speer, S. Rintoul, and S. Wijffels, 2010: Southern Ocean Thermocline Ventilation. *J. Phys. Oceanogr.*, **40,** 509-529.

Smith, W. H. and D. T. Sandwell, 1997: Global sea floor topography from satellite altimetry and ship depth soundings. *Science*, **277**, 1956-1962.

St. Laurent, L., and S. Merrifield, 2017: Measurements of Near-Surface Turbulence and Mixing from Autonomous Ocean Gliders. *Oceanogr.*, **30,** 116-125.

Accepted for publication in *Journal of Physical Oceanography.* DOI 10.1175/JPO-D-21-0015.1.

St. Laurent, L., A. C. Naveira Garabato, J. R. Ledwell, A. M. Thurnherr, J. M. Toole, and A. J. Watson, 2012: Turbulence and diapycnal mixing in Drake Passage. *J. Phys. Oceanogr.*, **42**, 2143-2152.

Sullivan, P. P., J. C. McWilliams, and W. K. Melville, 2007: Surface gravity wave effects in the oceanic boundary layer: large-eddy simulation with vortex force and stochastic breakers. *J. Fluid Mech.*, **593,** 405-452.

Sutherland, G., Christensen, K.H., Ward, B., 2014: Evaluating Langmuir turbulence parameterizations in the ocean surface boundary layer. *J. Geophys. Res. Oceans*, **119**, 1899-1910.

Sutherland, G., Marié, L., Reverdin, G., Christensen, K.H., Broström, G., Ward, B., 2016: Enhanced turbulence associated with the diurnal jet in the ocean surface boundary layer. J. Phys. Oceanogr., 46, 3051-3067.

Sutherland, G., Ward, B., Christensen, K. H., 2013: Wave-turbulence scaling in the ocean mixed layer. *Ocean Sci.,* **9**, 597-608.

Talley, L. D., 1996: Antarctic intermediate water in the South Atlantic. *The South Atlantic,* Springer, 219-238.

Terray, E. A., M. A. Donelan, Y. C. Agrawal, W. M. Drennan, K. K. Kahma, A. J. Williams, P.A. Hwan, and S. A. Kitaigorodskii, 1996: Estimates of kinetic energy dissipation under breaking waves. *J. Phys. Oceanogr.*, **26**, 792-807.

Thomson, J., M. S. Schwendeman, S. F. Zippel, S. Moghimi, J. Gemmrich, and W. E. Rogers, 2016: Wave-Breaking Turbulence in the Ocean Surface Layer. *J. Phys. Oceanogr.*, **46,** 1857-1870.

Thorpe, S. A, 2005: *The Turbulent Ocean*. Cambridge University Press, 439 pp.

Umlauf, L., H. Burchard, and K. Bolding, 2005: General Ocean Turbulence Model. Source Code Documentation, Baltic Sea Research Institute Warnemünde Technical Report, 346 pp.

Waterhouse, A. F., and Coauthors, 2014: Global patterns of diapycnal mixing from measurements of the turbulent dissipation rate. *J. Phys. Oceanogr.*, **44**, 1854-1872.

Wentz, F. J., J. Scott, R. Hoffman, M. Leidner, R. Atlas, and J. Ardizzone, 2015: Remote Sensing Systems Cross-Calibrated Multi-Platform (CCMP) 6-hourly ocean vector wind analysis product on 0.25 deg grid, Version 2.0. Remote Sensing Systems, Santa Rosa, CA, www.remss.com/measurements/ccmp.

Zippel, S. F., Farrar, J. T., Zappa, C. J., Miller, U., Laurent, L. S., Ijichi, T., Weller, R. A., McRaven, L., Nylund, S. and Le Bel, D., 2021: Moored turbulence measurements using pulse-coherent Doppler sonar. *J. Atmos. Ocean. Technol*.

TABLES

Buoyancy flux sign	**Depth ratio**	**Scaling**	**Profiles of**	**Regime**
$J_b < 0$		$\epsilon \approx u_*^3/kz$	700	Wind-Dominated
$0 < J_b$	$AML/L_{MO} < 1$		218	
	$1 < AML/L_{MO} < 10$	$\epsilon \approx 1.76u_*^3/kz + 0.58J_b$	7	Intermediate
	$10 < AML/L_{MO}$	$\epsilon \approx J_b$	0	Convection-Dominated
	No AML identified		7	

Table 1. Boundary layer similarity scaling (Lombardo & Gregg, 1989). Showing piecewise equation used to estimate TKE dissipation rate (ϵ) from water friction velocity (u_*) and buoyancy flux (J_b), with number of microstructure profiles described by each regime.

	ξ_5	ξ_4	ξ_3	ξ_2	ξ_1	ξ_0
Curve Fit $\mu(z)$	65.8318	-195.7996	217.5514	-109.1612	25.0325	-1.5199
PDF $\mu(z)$	67.0843	-199.1266	220.7982	-110.5756	25.2952	-1.5352
PDF $\sigma(z)$	-8.2071	37.8270	-67.6796	57.5501	-22.4064	3.9510

Table 2: Coefficients for bias polynomials (Eq. 7) given in Fig. 7.

Accepted for publication in *Journal of Physical Oceanography.* DOI 10.1175/JPO-D-21-0015.1.

FIGURES

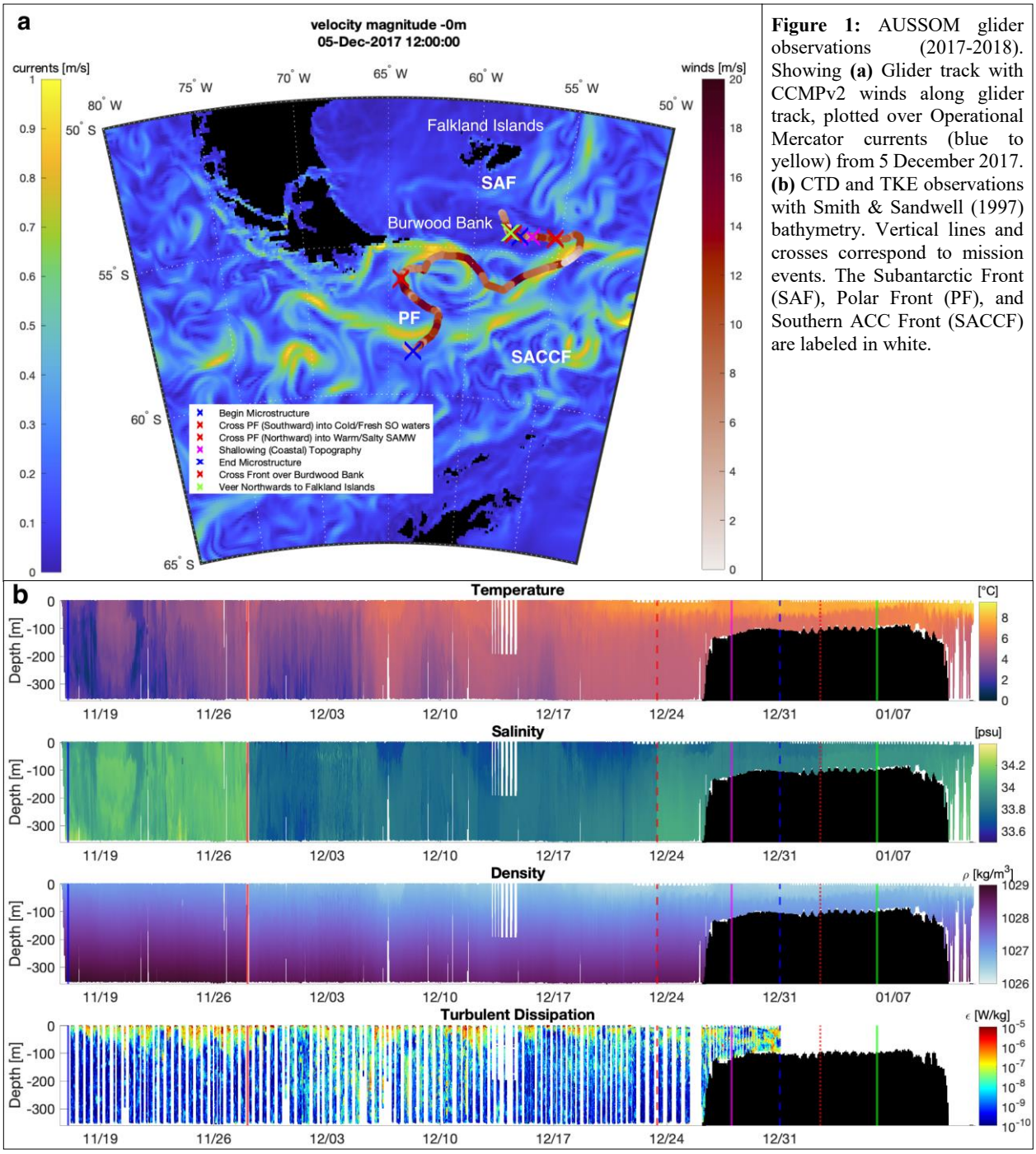

Figure 1: AUSSOM glider observations (2017-2018). Showing **(a)** Glider track with CCMPv2 winds along glider track, plotted over Operational Mercator currents (blue to yellow) from 5 December 2017. **(b)** CTD and TKE observations with Smith & Sandwell (1997) bathymetry. Vertical lines and crosses correspond to mission events. The Subantarctic Front (SAF), Polar Front (PF), and Southern ACC Front (SACCF) are labeled in white.

Accepted for publication in *Journal of Physical Oceanography.* DOI 10.1175/JPO-D-21-0015.1.

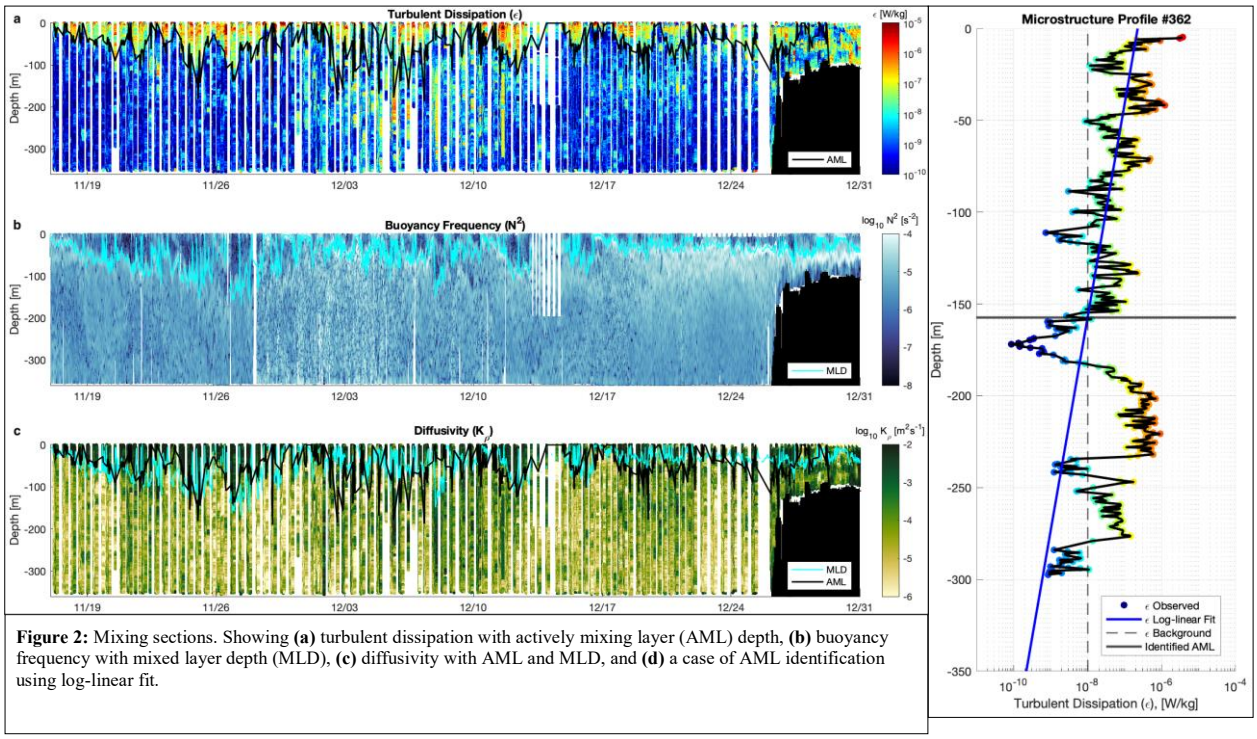

Figure 2: Mixing sections. Showing **(a)** turbulent dissipation with actively mixing layer (AML) depth, **(b)** buoyancy frequency with mixed layer depth (MLD), **(c)** diffusivity with AML and MLD, and **(d)** a case of AML identification using log-linear fit.

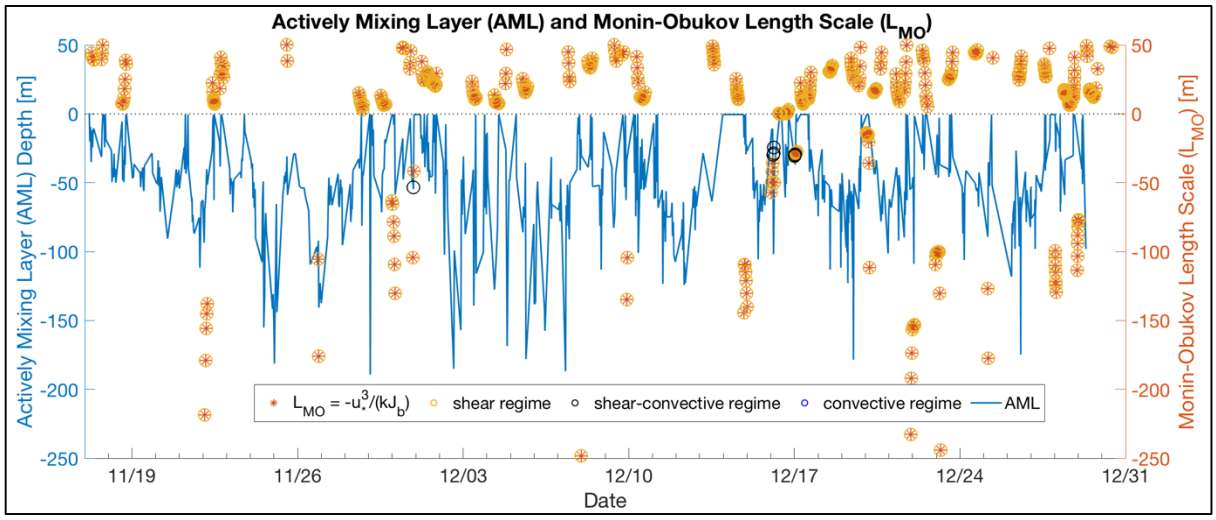

Figure 3: Monin-Obukhov length scale (LMO) in comparison to the actively mixing layer (AML). Note the y-axis has been limited from 50 to -250 meters to focus on those Monin-Obukhov length scales in proximity to the AML depth. There are 385 additional points above 50 meters (representing stabilizing buoyancy forcing) and 141 additional points below -250 meters (representing destabilizing-but-inconsequential buoyancy forcing).

Accepted for publication in *Journal of Physical Oceanography.* DOI 10.1175/JPO-D-21-0015.1.

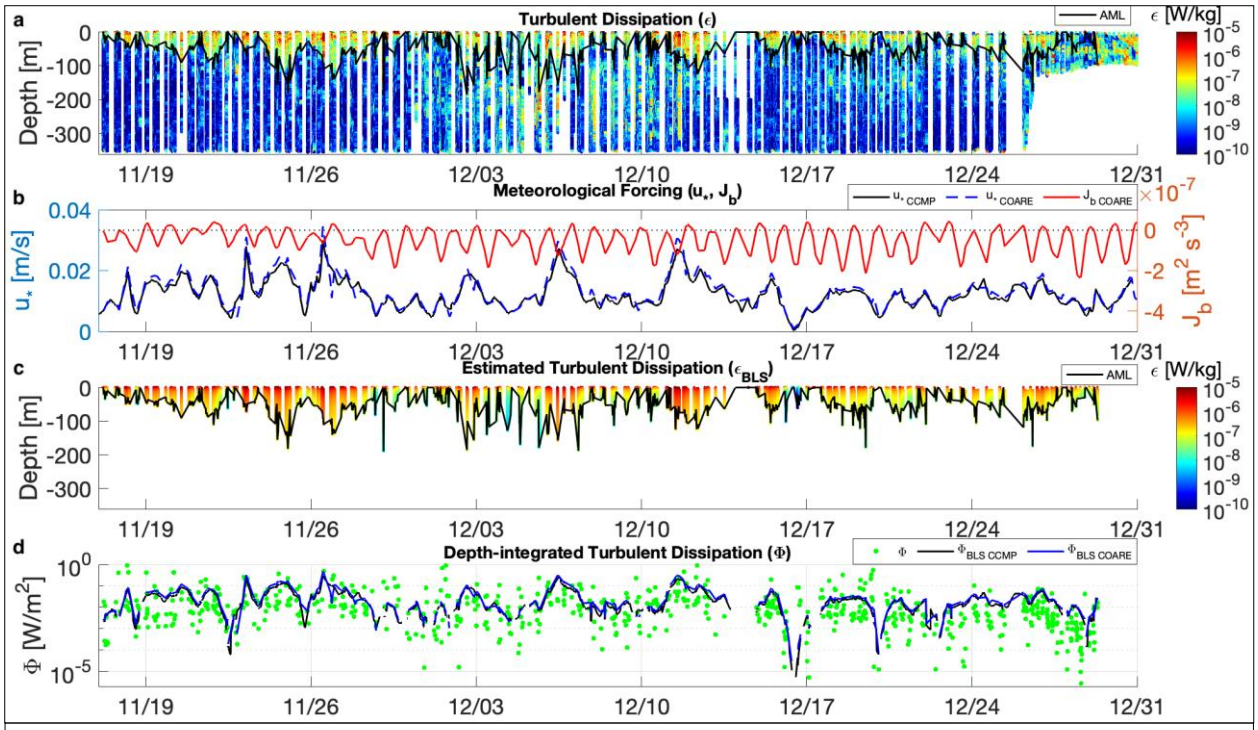

Figure 4: Boundary layer similarity scaling (BLS). Showing **(a)** observed turbulent dissipation with actively mixing layer (AML) depth, (b), direct meteorological forcing of near-surface turbulence including the full and wind-only estimate of u_*, (c) turbulent dissipation estimated using BLS, and (d) depth-integrated energy levels (units of flux) for each observed (green) and derived (blue and black) profile. Note that estimated turbulent dissipation section derived from COARE (wind and buoyancy flux) and CCMP (wind) are visually identical such that only the latter is shown.

Accepted for publication in *Journal of Physical Oceanography.* DOI 10.1175/JPO-D-21-0015.1.

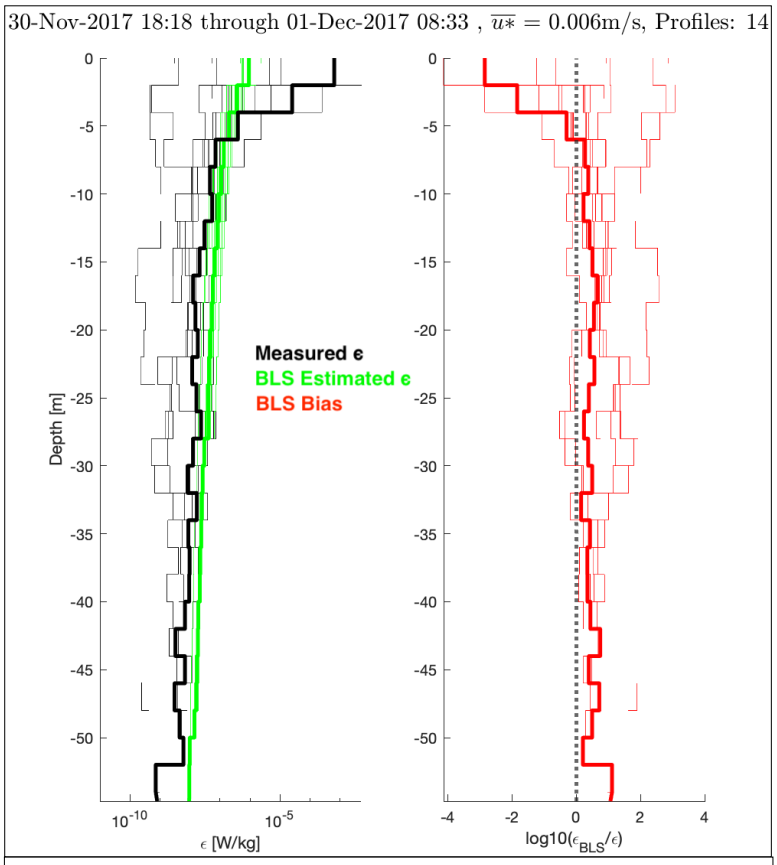

Figure 5: One centered interval of BLS, time-averaging (over inertial period) turbulent dissipation (left panel) and bias expressed as ratio of ϵ_{BLS} to measured ϵ (right panel) in depth space. Hereafter time-averaging is performed in AML-normalized (dimensionless) depth space. Averaged profiles are bold.

Accepted for publication in *Journal of Physical Oceanography.* DOI 10.1175/JPO-D-21-0015.1.

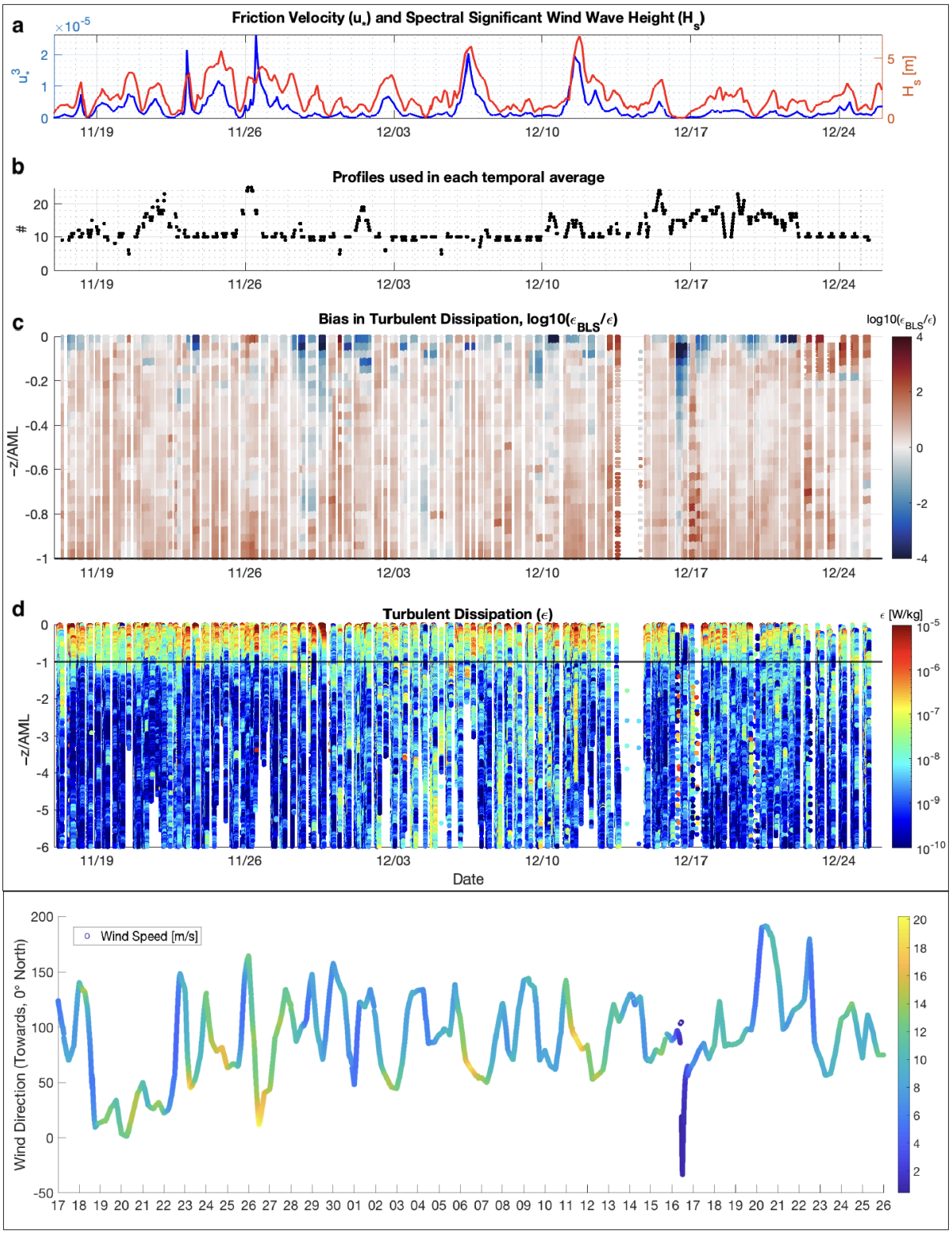

Figure 6: Bias of boundary layer similarity scaling (BLS). Showing (a) friction velocity u_* and windsea significant wave height H_s over glider, (b) availability of microstructure and associated BLS profiles for 14.5-hr temporal average, (c) BLS bias in the normalized AML, and (d) observed turbulent dissipation rates depth-normalized by the AML. Also showing (e) wind direction as a function of time, with 0º and 90º indicating wind towards the north and east, respectively, and total wind speed [m/s] as color axis.

Accepted for publication in *Journal of Physical Oceanography.* DOI 10.1175/JPO-D-21-0015.1.

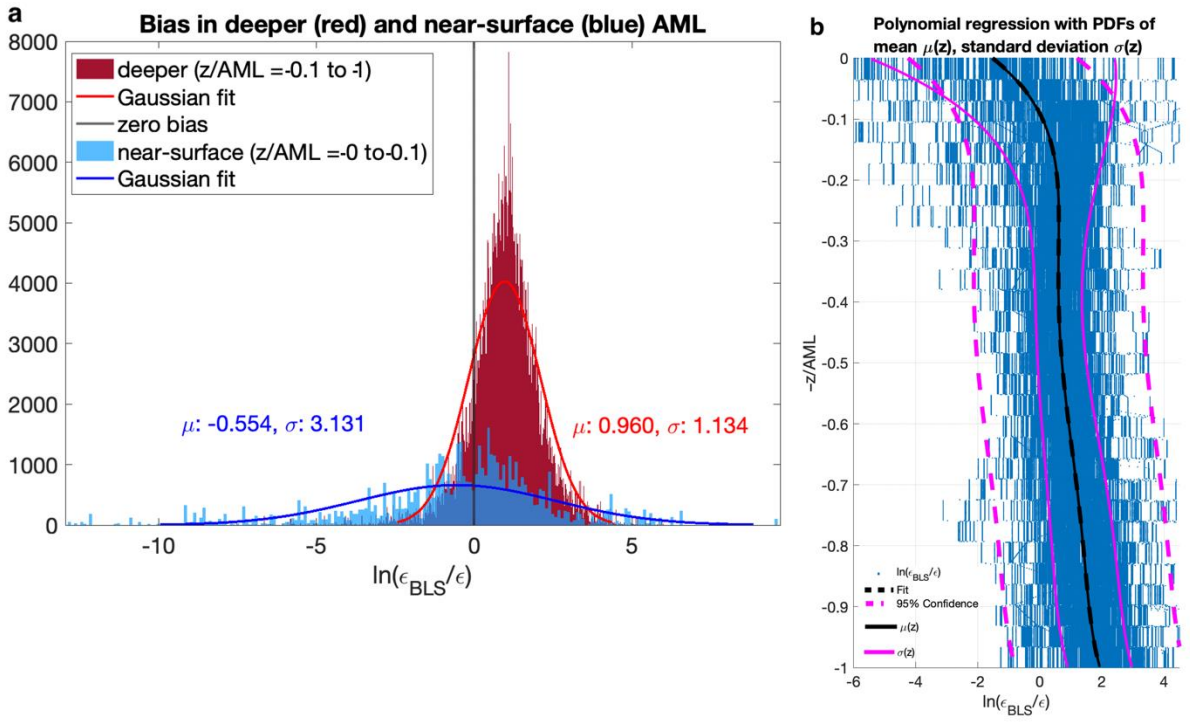

Figure 7: Histograms for bias in the **(a)** near-surface (blue) and deeper (red) AML. **(b)** Full dataset polynomial fit (dotted black) with 95% confidence intervals (dotted magenta). Additionally, polynomial fits for the mean (solid black) and standard deviation (solid magenta) of BLS bias are computed using a moving vertical window.

Accepted for publication in *Journal of Physical Oceanography.* DOI 10.1175/JPO-D-21-0015.1.

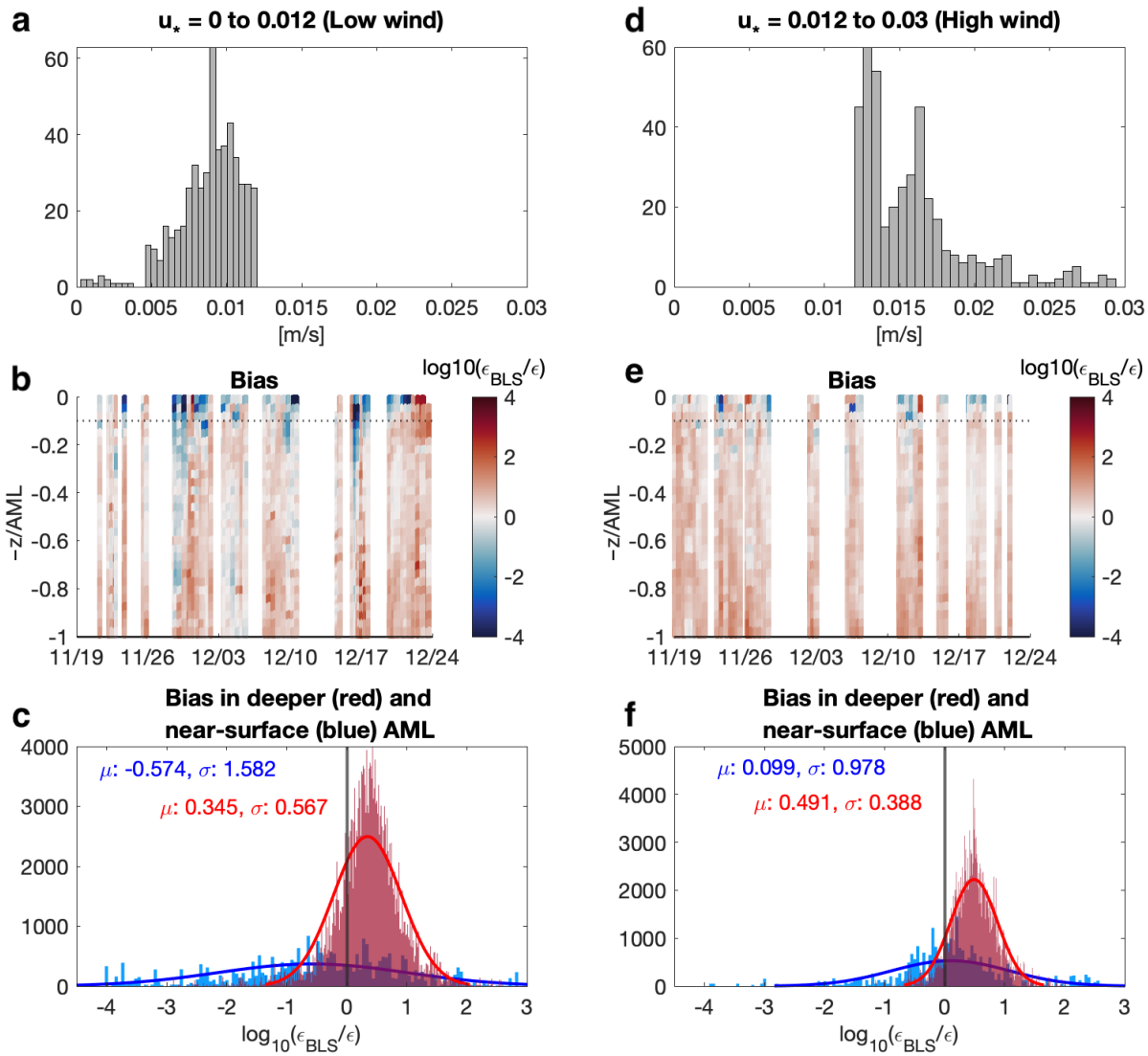

Figure 8: Histograms for BLS separated by water friction velocity (u_*) and position within the AML. **(a-c)** shows a bias section, near-surface histogram, and deeper AML histogram for low-wind conditions. **(d-f)** is the same for high-wind conditions. Near-surface and deeper regimes are separated by $\hat{z} = 0.1$ as in Fig. 7a.

Accepted for publication in *Journal of Physical Oceanography.* DOI 10.1175/JPO-D-21-0015.1.

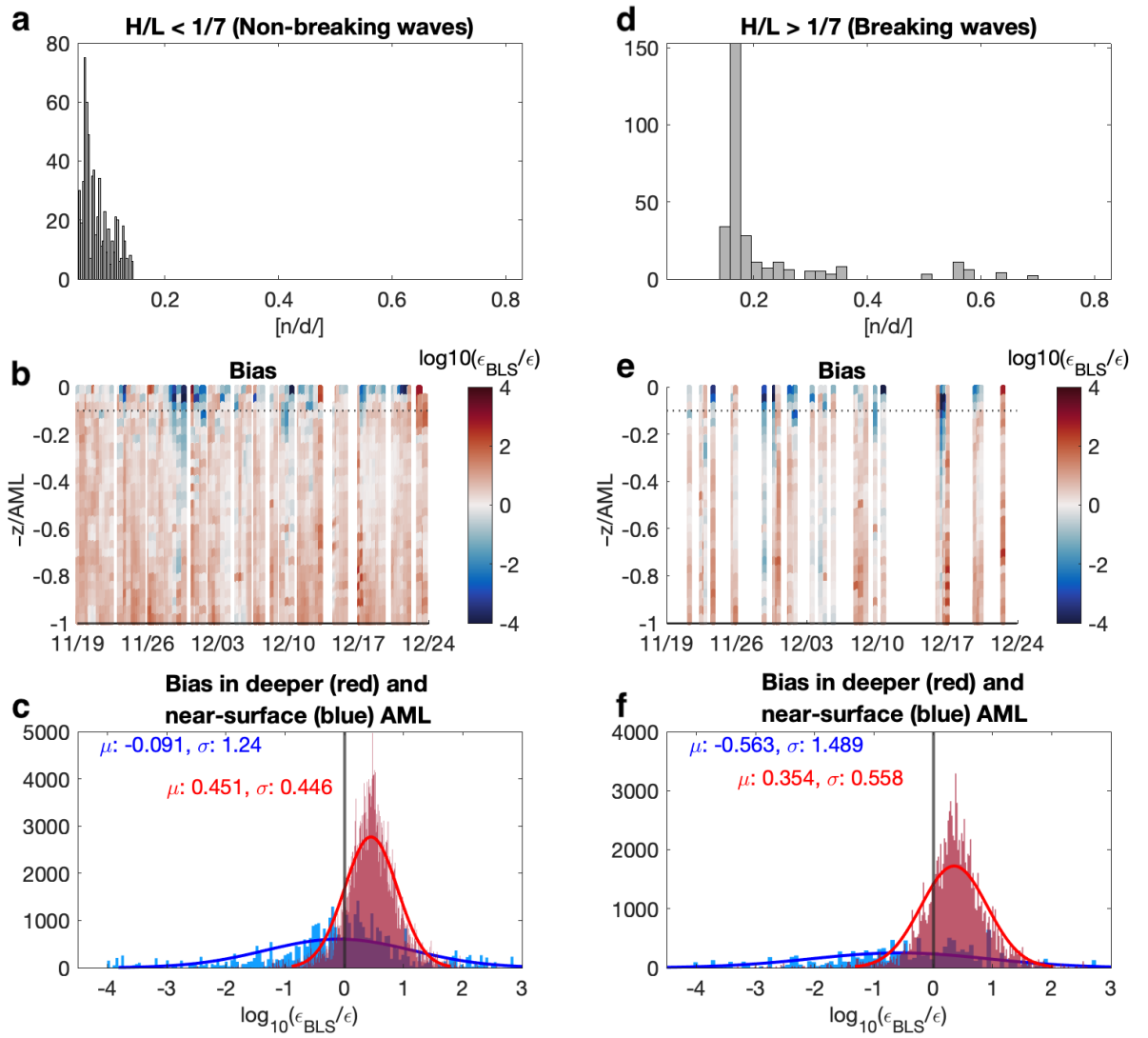

Figure 9: Histograms for BLS separated by wave steepness (H/L) and position within the AML. **(a-c)** shows a bias section, near-surface histogram, and deeper AML histogram for low-wind conditions. **(d-f)** is the same for high-steepness conditions. Near-surface and deeper regimes are separated by $\hat{z} = 0.1$ as in Fig. 7a.

Accepted for publication in *Journal of Physical Oceanography.* DOI 10.1175/JPO-D-21-0015.1.

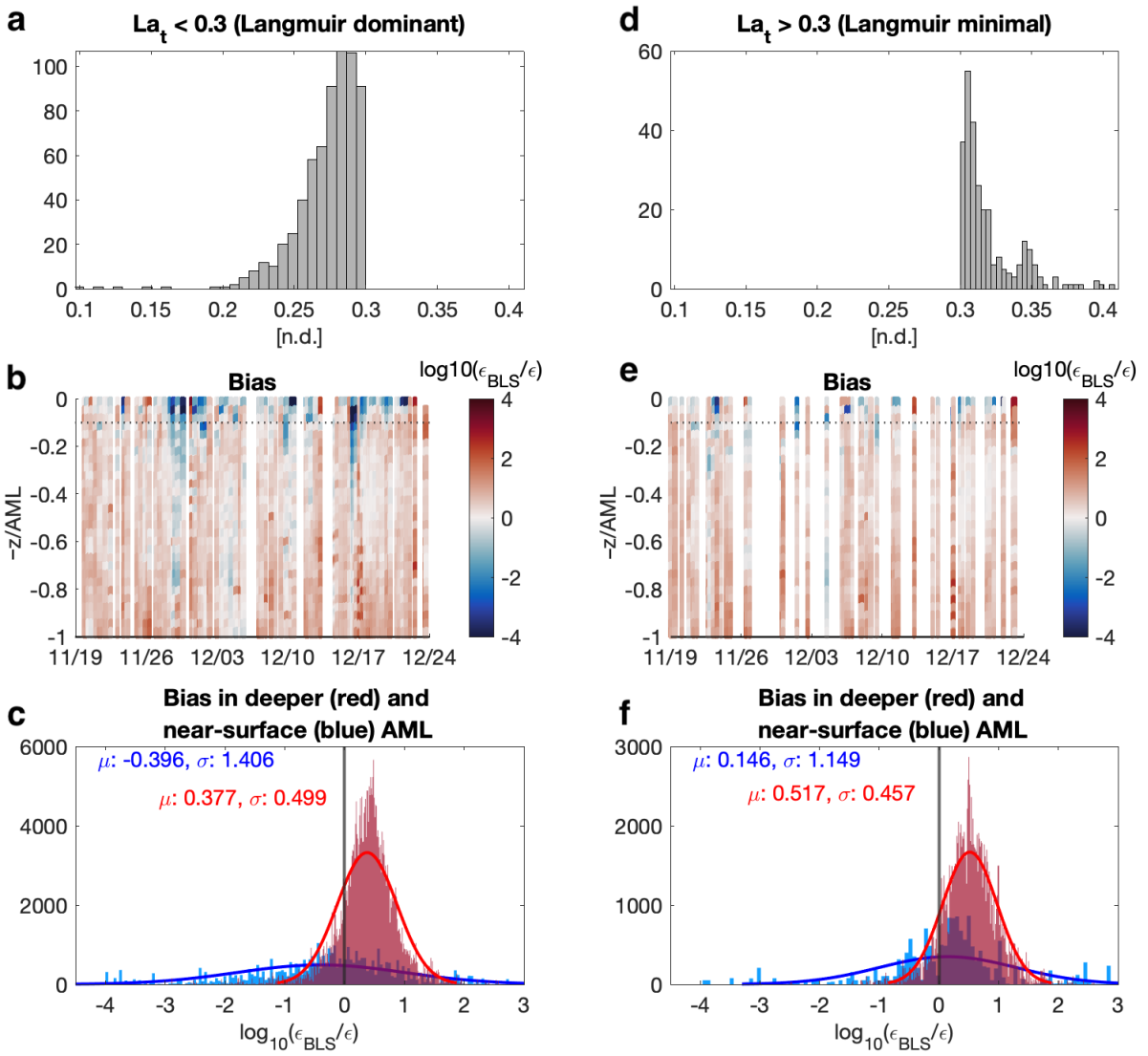

Figure 10: Histograms for BLS separated by whether conditions are conducive or not conducive to Langmuir circulation, as well as position within the AML. **(a-c)** shows a bias section, near-surface histogram, and deeper AML histogram for low-wind conditions. **(d-f)** is the same for Langmuir-stable conditions. Near-surface and deeper regimes are separated by $\hat{z} = 0.1$ in Fig. 7a.

Accepted for publication in *Journal of Physical Oceanography.* DOI 10.1175/JPO-D-21-0015.1.

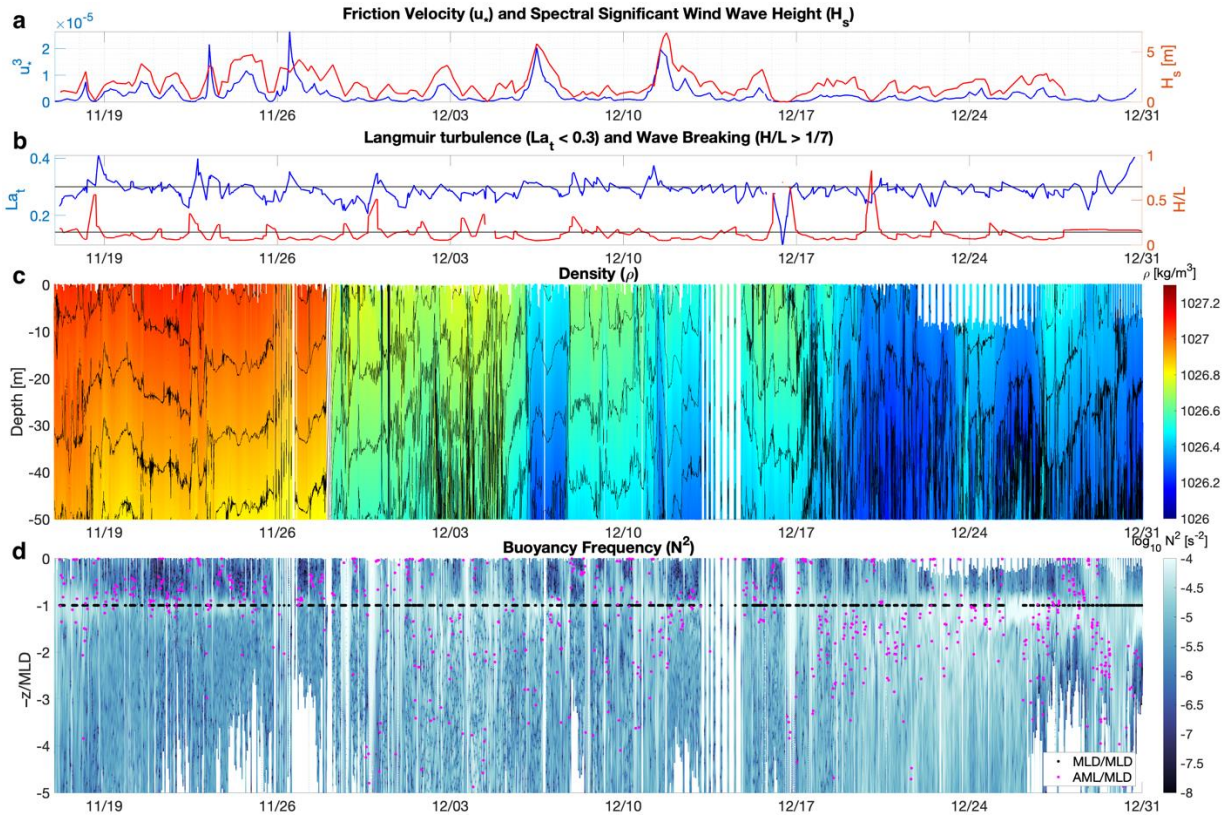

Figure 11: Near surface hydrography. Showing **(a)** friction velocity and significant wind wave height, **(b)** turbulent Langmuir number and wave steepness (H/L), **(c)** shallow density with isopycnal contours at 0.07 kg/m^3 intervals, and **(d)** stratification with AML and MLD depth-normalized by MLD.

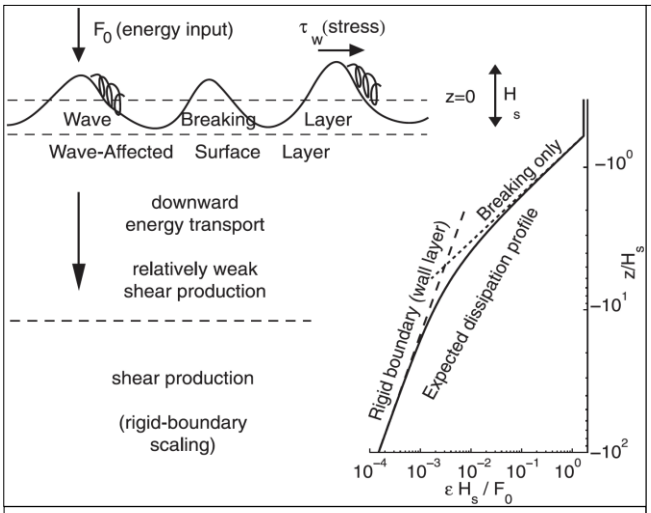

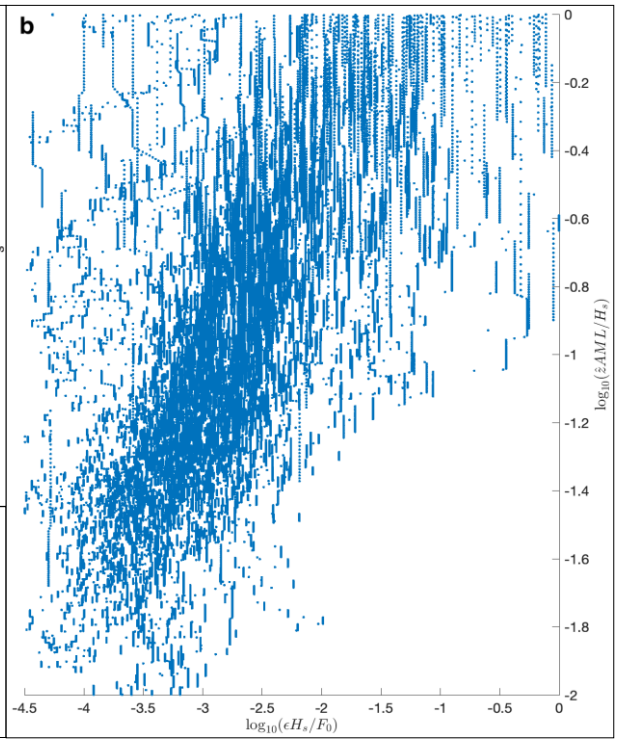

Figure 12: Boundary layer structure. Showing **(a)** cartoon schematic from Gerbi et al., (2009) and **(b)** the same figure constructed using AUSSOM glider microstructure dissipation measurements, windsea significant wave height H_s, and wind forcing $F_1 = -u_*^3 G_t$, where G_t is an empirical function of approximate wave age. Scatter (blue) includes 1 in 5 profiles for clarity.

Accepted for publication in *Journal of Physical Oceanography.* DOI 10.1175/JPO-D-21-0015.1.

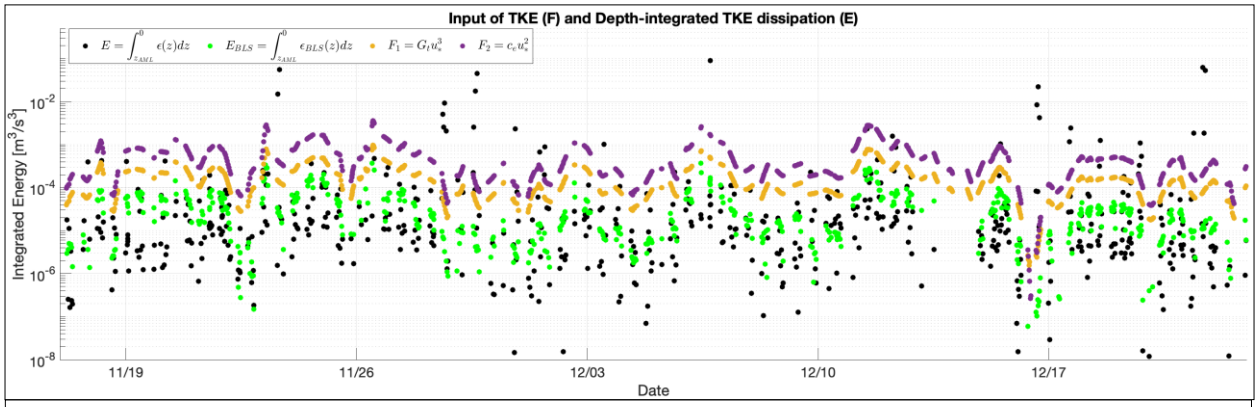

Figure 13: Depth-integrated TKE in comparison to inputs of TKE from wind estimated by alternative scalings. G_t is an empirical function of wave age (Terray et al., 1996) which ranges from 37 to 182 for our dataset. Wave age is calculated using an approximation of data published in Edson et al. (2013), given by $u_{*a}/c_p \approx 0.004U_{10} - 0.003$ (Edson, pers. comm, Nov. 2020). Effective energy transfer velocity $c_e \approx 0.148U_{10} + 1.11$ is calculated after Hwang (2009) and is generally 1.5 to 3 m/s in the ocean.